ARTICLE

doi:10.1038/nature13406

Structure of an Rrp6–RNA exosome complex bound to poly(A) RNA

Elizabeth V. Wasmuth[1,2], Kurt Januszyk[1] & Christopher D. Lima[1,3]

The eukaryotic RNA exosome processes and degrades RNA by directing substrates to the distributive or processive 3′ to 5′ exoribonuclease activities of Rrp6 or Rrp44, respectively. The non-catalytic nine-subunit exosome core (Exo9) features a prominent central channel. Although RNA can pass through the channel to engage Rrp44, it is not clear how RNA is directed to Rrp6 or whether Rrp6 uses the central channel. Here we report a 3.3 Å crystal structure of a ten-subunit RNA exosome complex from *Saccharomyces cerevisiae* composed of the Exo9 core and Rrp6 bound to single-stranded poly(A) RNA. The Rrp6 catalytic domain rests on top of the Exo9 S1/KH ring above the central channel, the RNA 3′ end is anchored in the Rrp6 active site, and the remaining RNA traverses the S1/KH ring in an opposite orientation to that observed in a structure of a Rrp44-containing exosome complex. Solution studies with human and yeast RNA exosome complexes suggest that the RNA path to Rrp6 is conserved and dependent on the integrity of the S1/KH ring. Although path selection to Rrp6 or Rrp44 is stochastic *in vitro*, the fate of a particular RNA may be determined *in vivo* by the manner in which cofactors present RNA to the RNA exosome.

The eukaryotic RNA exosome core is an essential nine-subunit complex formed by two stacked rings of six RNase PH-like proteins on the bottom and three S1/KH domain 'cap' proteins on the top. Exo9 associates with the endo- and 3′ to 5′ processive exoribonuclease Rrp44, and the 3′ to 5′ distributive exoribonuclease Rrp6 (ref. 1). In *Saccharomyces cerevisiae*, the cytoplasmic exosome includes Exo9 and Rrp44 ($Exo10^{Rrp44}$), the nuclear exosome contains Exo9, Rrp44 and Rrp6 ($Exo11^{Rrp44/Rrp6}$)[2], and a nucleolar exosome with Exo9 and Rrp6 ($Exo10^{Rrp6}$) has been posited in human[3]. Each exosome complex may be uniquely equipped to target different RNA substrates, in conjunction with protein cofactors, to catalyse RNA turnover, quality control, or processing in the context of their respective cellular compartments[4].

Rrp6 is a RNase D family member[5], and is proposed to hydrolyse RNA via two metal ion catalysis[6,7]. It includes an amino-terminal PMC2NT domain that associates with a cofactor Rrp47 (ref. 8), an exoribonuclease domain (EXO), an HRDC domain, and a carboxy-terminal domain (CTD) that associates with the Exo9 core[9]. Structural studies revealed that the EXO and HRDC domains constitute the catalytic module[10,11] and a $Exo10^{Rrp44+Rrp6Cterm}$ structure revealed how Rrp6 CTD residues interact with Exo9 (ref. 12). No structures yet exist for Rrp6 in complex with Exo9 or RNA.

We proposed that Rrp44 and Rrp6 use an overlapping channel within the S1/KH ring to engage RNA, that Rrp6 activities are modulated by Exo9, and that Rrp6 stimulates Rrp44 in binding and degradation of single stranded RNA in the context of $Exo11^{Rrp44/Rrp6}$ (ref. 13). To provide a structural basis for these observations, we crystallized Rrp6 with Exo9 and a 24-nucleotide single-stranded poly(A) RNA ($poly(A)_{24}$ RNA).

Global architecture of $Exo10^{Rrp6}$–poly(A) RNA

The 3.3 Å structure of $Exo10^{Rrp6}$ was obtained in the presence of a 24-nucleotide (nt) single-stranded poly(A) RNA using Rrp6 (128–685) that lacked exoribonuclease activity (D238N)[13,14], the PMC2NT domain (1–127)[13] and its last 48 C-terminal residues (Extended Data Fig. 1; Extended Data Table 1). Rrp6 is positioned atop the Exo9 S1/KH ring with Exo9 subunits resembling those of human Exo9 (ref. 15) and yeast Exo9 (ref. 12) in $Exo10^{Rrp44+Rrp6Cterm}$ (Fig. 1a, b). $Poly(A)_{24}$ RNA is coordinated within the S1/KH ring with Rrp6 active site residues contacting the RNA 3′ end (Fig. 1c). The Rrp6 EXO domain contacts two of the three S1/KH ring proteins, Rrp4 and Rrp40, and the HRDC domain is proximal to Rrp4, although no direct contacts are apparent. Consistent with previous results[12], the Rrp6 CTD wraps around the N-terminal domain (NTD) of Csl4 and PH-like subunit, Rrp43, before emerging at the top of the Exo9 core (Fig. 1a; Extended Data Fig. 2a, b). No electron density was observed for CTD residues 629–684 and for residues (517–524) that link the HRDC domain and CTD. The location of the Rrp6 N terminus (Met 128) places the Rrp6 PMC2NT domain over the Exo9 central channel in an ideal position to interact with Rrp47 to facilitate substrate recruitment (Fig. 1a). Alignment of exosome-associated Rrp6 to the yeast Rrp6 catalytic module (EXO-HRDC) reveals few differences (Extended Data Fig. 2c).

The NTD of Rrp4 and S1 domains of Rrp4 and Rrp40 interact with the Rrp6 EXO domain, burying 2,230 $Å^2$ of surface area in the complex. Rrp6 interactions with the Rrp4 NTD (Region 2) and S1 domain (Region 3) are more extensive (1,750 $Å^2$), whereas interactions with the Rrp40 S1 domain and Rrp4 S1 domain encompass a region proximal to the RNA binding site (Region 1). These surfaces are highly conserved (Fig. 2a, b) in comparison to the Rrp6 CTD (Extended Data Fig. 2a), which is important for Rrp6 interaction with the exosome core as illustrated by analytical gel-filtration studies showing that the CTDs of both yeast and human Rrp6 are required for association with the exosome (Extended Data Fig. 3).

The structure of $Exo10^{Rrp6}$ bound to $poly(A)_{24}$ RNA reveals how an RNase D family member interacts with RNA (Fig. 2c). The Rrp6 catalytic domain and active site bind $A_{21}A_{22}A_{23}A_{24}$ with the 2′-OH and 3′-OH of the terminal A_{24} coordinated via two main-chain hydrogen bonds to the backbone amide and carbonyl oxygen of His 241 and Glu 240 side-chain carboxylate, similar to that observed for AMP in the Rrp6 catalytic domain[10]. An additional contact is observed to A_{24} between the N7 adenine atom and Gln 345 side chain amide. The scissile phosphate of A_{24} and A_{23} is coordinated by a single magnesium ion that bridges

[1]Structural Biology Program, Sloan-Kettering Institute, 1275 York Avenue, New York, New York 10065, USA. [2]Louis V. Gerstner Jr. Graduate School of Biomedical Sciences, Sloan-Kettering Institute, Memorial Sloan-Kettering Cancer Center, 1275 York Avenue, New York, New York 10065, USA. [3]Howard Hughes Medical Institute, 1275 York Avenue, New York, New York 10065, USA.

©2014 Macmillan Publishers Limited. All rights reserved

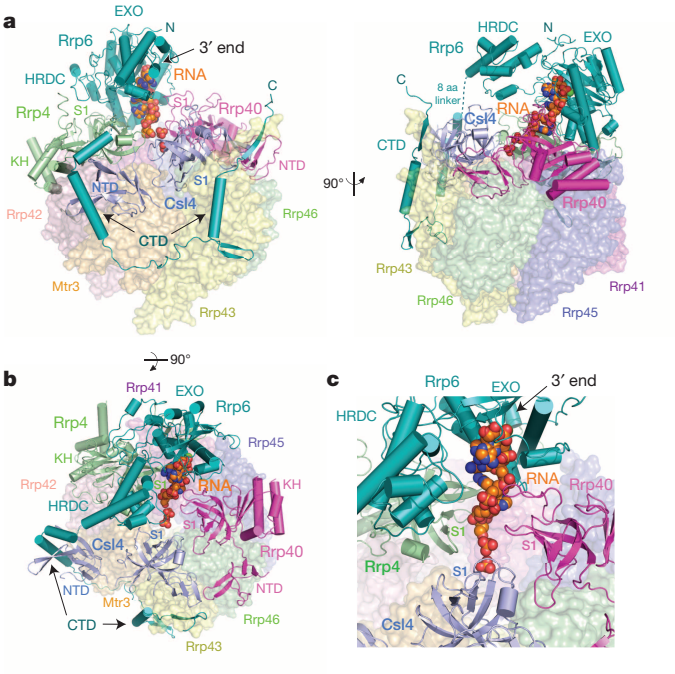


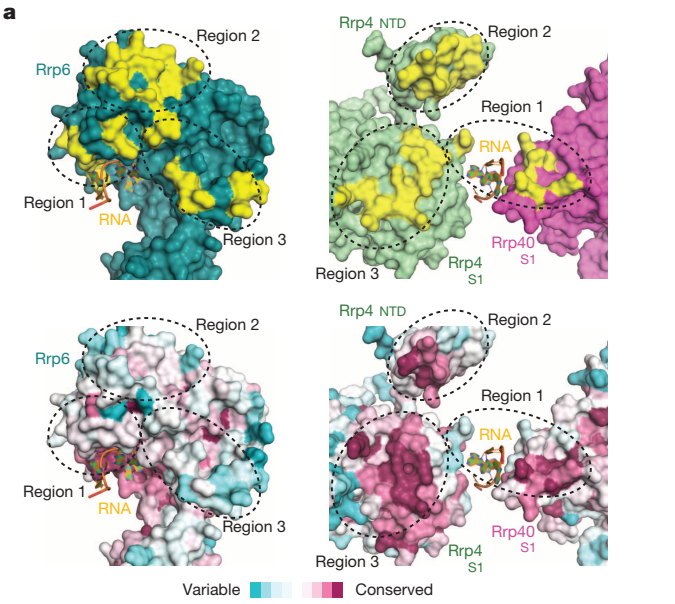
Figure 1 | Overall structure of a RNA bound Rrp6 exosome. **a**–**c**, Cartoon and surface representation of *S. cerevisiae* Exo10^{Rrp6} bound to poly(A)$_{24}$ RNA. Views from the sides (**a**), top (**b**) and close-up (**c**) of RNA engaged by the Rrp6 EXO domain and S1 domains of Rrp40, Rrp4 and Csl4. RNase PH-like ring as transparent surfaces, S1/KH ring and Rrp6 as cartoons, RNA as spheres.

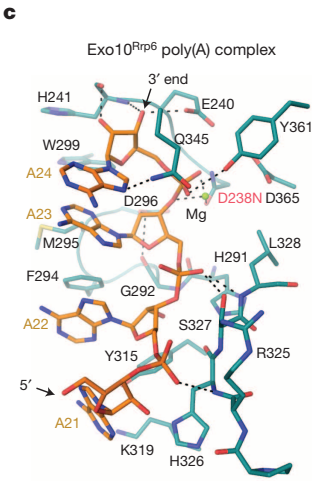
the phosphate and the side chain carbonyl of Asn 238 (Asp in wild-type enzyme). The scissile phosphate is within hydrogen bond distance of the invariant side chain hydroxyl of Tyr 361 (Extended Data Fig. 4a,c). Consistent with the proposed reaction mechanism[7], two metal ions coordinated by conserved side-chain carboxylates in the yeast Rrp6–AMP complex are ideally positioned to contact the scissile phosphate (Extended Data Fig. 4c, d). Several contacts between metal ions and RNA are missing in our structure owing to the D238N substitution.

The remaining contacts to poly(A)$_{24}$ RNA reveal several non-specific interactions, consistent with the ability of Rrp6 to degrade RNA of any sequence. A$_{23}$ 2′-OH is within hydrogen-bonding distance to the side-chain carboxylate of Asp 296, whereas the A$_{23}$ phosphate is within hydrogen-bonding distance of the Leu 328 backbone amide. The A$_{23}$ base is situated over the A$_{24}$ base with van der Waals contacts provided by side chains of Trp 299, Met 295 and Phe 294. Phe 294 is positioned between the A$_{23}$ and A$_{22}$ bases, presumably disrupting base-stacking interactions. The A$_{22}$ base and ribose are cradled by van der Waals contacts to Phe 294, Gly 292, His 291 and Tyr 315 while its phosphate is within hydrogen bonding distance with the backbone amide of His 291. Lys 319, His 326 and Tyr 315 contribute the remaining contacts to the A$_{21}$ base. Importantly, none of the aforementioned contacts seem to interrogate the identity of the base. Sixteen of eighteen residues observed in direct contact to the RNA or metal cofactors are conserved in human RRP6 (Extended Data Fig. 4a, b)[10,11].

RNA passes through the S1/KH ring

Four out of six nucleotides of poly(A)$_{24}$ RNA observed in electron density (5′-A$_{19}$-A$_{24}$-3′) are coordinated by Rrp6 placing the 5′ end (A$_{19}$) proximal to conserved, basic side chains from Rrp4 (Lys 122 and Arg 123),





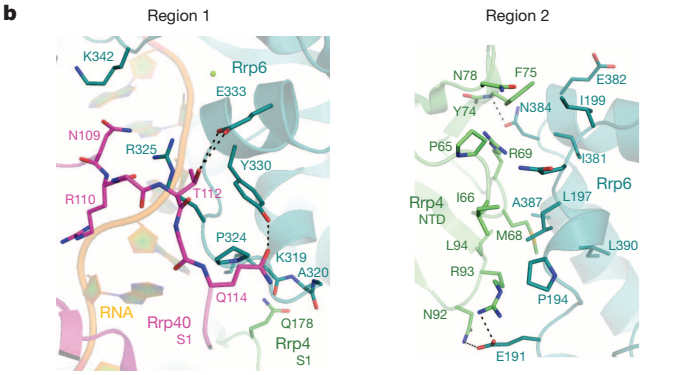


Figure 2 | Rrp6 contacts the S1/KH ring and RNA. **a**, **b**, Rrp6 EXO domain interface with Rrp4 and Rrp40 as yellow buried surfaces (**a**) and in atomic detail (**b**). **a**, Top, Rrp6 (teal; left), Rrp4 (pale green; right) and Rrp40 (magenta; right) in open-book representation (160°). Bottom, surfaces coloured by sequence conservation from red (conserved) to blue (variable). **b**, Contacts between Rrp6, Rrp4 and Rrp40 in stick representation coloured as in **a**. **c**, Contacts between RNA (orange), magnesium (green) and Rrp6 active site residues (teal) in Exo10$^{Rrp6–RNA}$. A catalytic aspartate, D238, is mutated (D238N; red). Potential hydrogen bonds depicted as dashed lines.

©2014 Macmillan Publishers Limited. All rights reserved

while Rrp40 Lys 108 points towards A_{24} and Arg 110 is proximal to the phosphate of A_{21} and ribose of A_{20} (Fig. 3a). Additional densities with spacing consistent with the RNA phosphate backbone, modelled as PO_{4a} and PO_{4b}, are observed within the S1/KH ring nearest to Arg 150 and proximal to Arg 145 and Arg 202 of Csl4 (Extended Data Fig. 1a–c). The aforementioned Csl4, Rrp4 and Rrp40 residues are highly conserved[15]. No additional density consistent with RNA is observed within the PH-like ring.

Rrp6 and Rrp44 use a shared portion of the central channel to engage RNA substrates[13], and alignment of Exo10^{Rrp6} and Exo10$^{Rrp44+Rrp6Cterm}$ reveals overlapping paths for RNA within the S1/KH central channel (Fig. 3a, b), albeit in opposing directions. A subset of side chains from the S1/KH cap proteins contact RNA in both structures, but none make contacts that would enforce directionality. To determine the importance of the S1/KH ring for RNA degradation, yeast Exo10^{Rrp6} and Exo11$^{Rrp44/Rrp6}$ were reconstituted with Csl4 and Rrp40 containing amino acid substitutions for Arg 145, Arg 150 and Arg 202 in Csl4, and for Lys 107, Lys 108 and Arg 110 in Rrp40. These mutations severely diminish Rrp6 activity in Exo10^{Rrp6} and Exo11$^{Rrp44/Rrp6}$ as well as Rrp44 activity in Exo11$^{Rrp44/Rrp6}$ (Fig. 3c; Extended Data Fig. 5a). In contrast, Rrp6 activity is not inhibited by an insertion in Rrp45 that occludes the PH-like ring channel below the S1/KH ring[13], although this mutation inhibits Rrp44 activity. Reconstituted human Exo10^{RRP6} (Extended Data Fig. 3b) reveals similar dependencies as a channel-occluding insertion in RRP41 near the S1/KH ring impaired RRP6 activity, whereas a channel-occluding insertion in RRP45 well below the S1/KH ring failed to inhibit RRP6 (Fig. 3d; Extended Data Fig. 5b). Combining insertions inhibits RRP6 to a greater degree, probably because the RRP45 insertion restricts movement of the RRP41 insertion. These data indicate that the RNA path to Rrp6 depends on the integrity of the S1/KH ring, but does not require the full extent of the PH-like ring central channel. In contrast, at least for yeast Exo11$^{Rrp44/Rrp6}$, the RNA path to Rrp44 relies on the integrity of central channel throughout both S1/KH and PH-like rings. These data are consistent with contacts observed to RNA in structures of Exo10^{Rrp6} and Exo10$^{Rrp44+Rrp6Cterm}$.

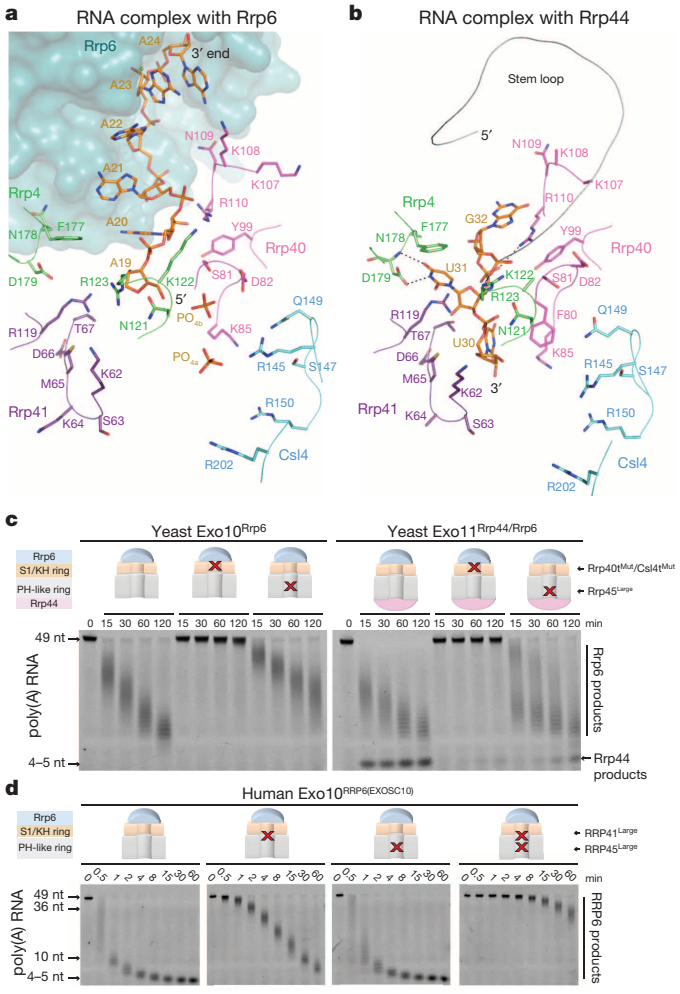


Figure 3 | Rrp6 activities are dependent on the S1/KH ring. **a**, **b**, Partially overlapping paths for RNA in complex with Exo10^{Rrp6} (**a**) and Exo10$^{Rrp44+Rrp6Cterm}$ (**b**) within the S1/KH ring. RNA and S1/KH side chains depicted as sticks, Rrp6 as a surface (**a**), the stem loop in Exo10$^{Rrp44+Rrp6Cterm}$ as a ribbon (**b**). Colour-coded labels adjacent to subunits. **c**, RNA decay activities for yeast Exo10^{Rrp6} and Exo11$^{Rrp44/Rrp6}$ with mutations in the S1/KH ring or a channel occluding insertion lower in the PH-like ring (Rrp45^{Large}). **d**, RNA decay activities for human Exo10^{RRP6} with insertions at the top (RRP41^{Large}) or middle of the PH-like ring (RRP45^{Large}). RNA decay assays were conducted at least three times for each of the samples with typical results depicted in **c** and **d**.

To map RNA interactions through Exo9 to Rrp6 and Rrp44, catalytically dead yeast exosome complexes were reconstituted and subjected to long-wavelength ultraviolet crosslinking using 36-nt poly(A) or AU-rich RNA substrates bearing single 4-thioU substitutions 6, 21 or 29 nt from the 3′ end (Fig. 4a, Extended Data Fig. 6a–c). As the 4-thioU probe is moved 3′ to 5′, AU-rich RNA crosslinks to Rrp44, followed by the PH-like ring, and finally to the S1/KH cap in Exo10^{Rrp44} and Exo11$^{Rrp44/Rrp6}$, in agreement with previous studies[12,13,16,17]. In contrast, crosslinks are only observed to Rrp44 in Exo10^{Rrp44} with poly(A)$_{36}$ RNA; however, addition of Rrp6 in Exo11$^{Rrp44/Rrp6}$ results in crosslinks that progress from Rrp44 through the PH-like ring to the S1/KH ring and Rrp6 as the 4-thioU probe is moved 3′ to 5′. The results with poly(A)$_{36}$ RNA are in line with previous biochemistry showing that Rrp6 stimulates Rrp44 binding to poly(A) RNA in Exo11$^{Rrp44/Rrp6}$ (ref. 13).

Crosslinking to the Exo10^{Rrp6} complex reveals RNA contacts to Rrp6 and Rrp4 when 4-thioU is 6 nt from the 3′ end. Although no structural impediment exists to prevent RNA from entering the PH-like ring, poly(A)$_{36}$ and AU-rich RNA crosslinks are only observed to Rrp4, Csl4 and Rrp40 even when the 4-thioU is positioned 21 or 29 nt from the 3′ end (Fig. 4c; Extended Data Fig. 6). This pattern contrasts with that observed for Exo10^{Rrp44} and Exo11$^{Rrp44/Rrp6}$, where crosslinks are observed to PH-like ring subunits when 4-thioU is placed 21 nt from the 3′ end. Crosslinking patterns to human Exo10^{RRP6} used a 36-nt AU-rich substrate as reported previously[13]. Similar to results obtained for yeast, ultraviolet-induced crosslinks are observed to the three S1/KH ring proteins and RRP45, but to none of the other five PH-like proteins (Fig. 4b). Ultraviolet crosslinking to complexes with loop insertions mirror results observed in decay assays (Fig. 3d) with diminished crosslinking when a loop insertion is placed proximal to the S1/KH ring (Extended Data Fig. 7). These data indicate that the integrity of the S1/KH ring central channel is important for Rrp6 activity in both human and yeast systems.

The results are consistent with a model in which distinct but overlapping paths guide RNA to Rrp6 or to Rrp44 (Fig. 4c). So how is a path selected? Path selection seems stochastic *in vitro* because degradation products of Rrp6 and Rrp44 are observed under conditions of limiting enzyme (Fig. 3c) or limiting substrate (Fig. 4d). The distributive mechanism underlying Rrp6 activity suggests repeated substrate binding and release, whereas the processive mechanism used by Rrp44 suggests that it binds and holds onto substrates until completely degraded. Thus at steady state, binding and ultraviolet crosslinking probably reflect the stable interaction with Rrp44 even when Rrp6 is present[13] (Extended Data Fig. 6a). Additional evidence for stochastic sampling of the two paths is evident by ultraviolet crosslinking under conditions of slight enzyme excess (Fig. 4d). As predicted based on the distributive and processive mechanisms of Rrp6 and Rrp44, respectively, crosslinked products are observed to Rrp44, Rrp6 and the S1/KH ring proteins at the earliest times, and this pattern is lost once most of the RNA finds its way to the Rrp44 active site.

Structural analysis of the Exo10^{Rrp6} poly(A) complex suggests at least four potential paths past the S1/KH ring to Rrp6, although paths 1 and 2

©2014 Macmillan Publishers Limited. All rights reserved

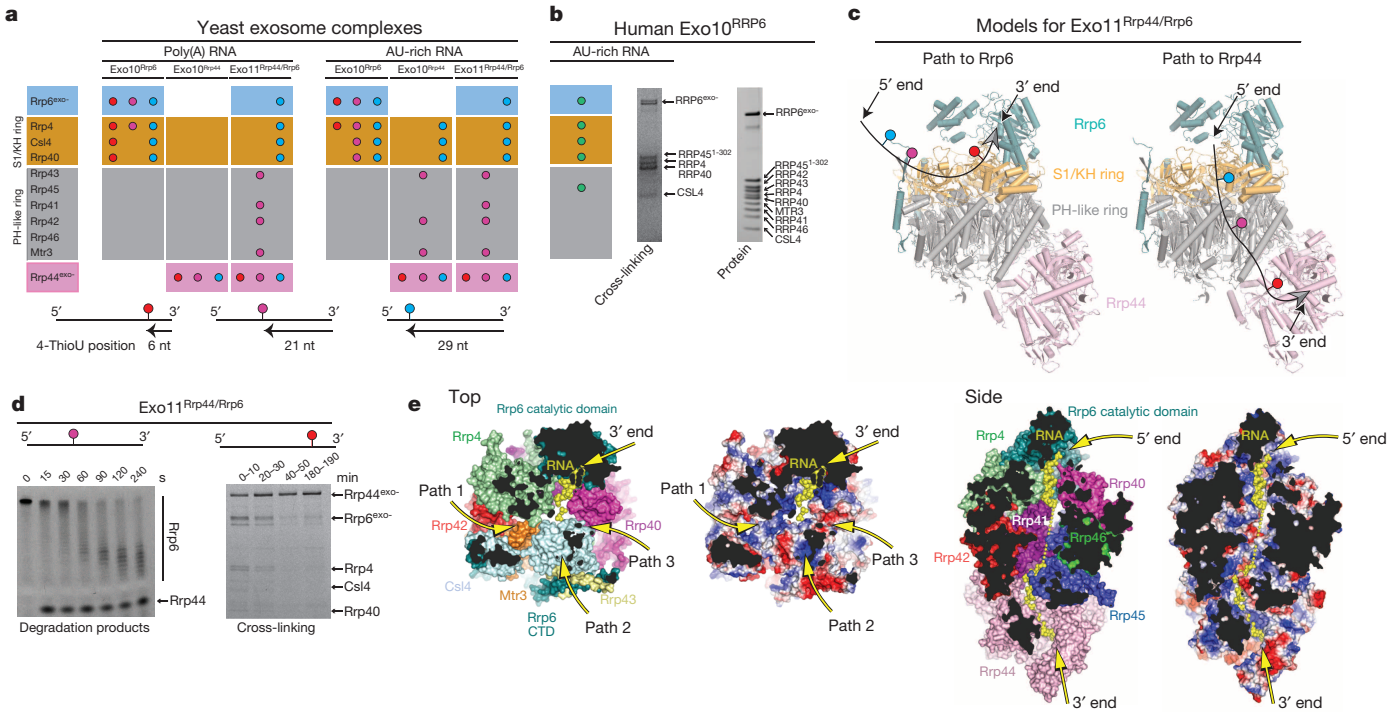


Figure 4 | RNA paths to Rrp6 and Rrp44. **a**, RNA crosslinking pattern schematic for yeast exosomes (Extended Data Fig. 6a). Subunits labelled, background coloured with Rrp6 (blue), S1/KH ring (orange), PH-like ring (grey) and Rrp44 (pink). 4-thioU positions indicated by coloured circles at 6, 21 or 29 nt from the 3′ end. **b**, RNA crosslinking pattern schematic for human Exo10^{RRP6} as in **a**. Crosslinks (left); proteins (right) (Extended Data Fig. 7). **c**, Exo11$^{Rrp44/Rrp6}$ cartoon. Subunits and rings coloured and labelled. RNA paths depicted by arrows, arrowhead at 3′ end with 4-thioU positions indicated as in **a**. **d**, RNA degradation at fivefold enzyme excess with Rrp6 and Rrp44 products (left) and time course for crosslinking to 4-thioU RNA 6 nt from 3′ end (right). **e**, Exo11$^{Rrp44/Rrp6}$ model indicating RNA paths to Rrp6 (left) or Rrp44 (right). Subunits coloured as in Fig. 1 next to surfaces coloured according to electrostatic potential[27]. Visible subunits and RNA (yellow) labelled in left panels. Three putative paths past the S1/KH ring to Rrp6 denoted by yellow arrows (Extended Data Fig. 8a). Side view shows an RNA path to Rrp44 (yellow arrow; 5′ and 3′ ends labelled) indicating that RNA could pass by Rrp6 (Extended Data Fig. 8b). RNA from PDB 4IFD was edited to remove the stem loop after nt 36. Assays in **a**, **b**, **d** conducted at least three times with typical results depicted.

seem most likely with respect to electrostatics and conservation (Fig. 4e; Extended Data Fig. 8a). Importantly, these paths are available in Exo11$^{Rrp44/Rrp6}$ as they do not involve surfaces from the PH-like ring or Rrp44. Modelling Rrp6 onto the Exo10^{Rrp44} RNA complex shows that the central channel is still accessible and that RNA paths to Rrp6 and Rrp44 are available in Exo11$^{Rrp44/Rrp6}$ (Fig. 4e; Extended Data Fig. 8b).

A wider channel in Exo10^{Rrp6}

Rrp6 can stimulate Rrp44 binding and decay activities[13], a phenomenon readily apparent in crosslinking to poly(A) RNA (Fig. 4a; Extended Data Fig. 6a). These results indicate that Rrp6 enhances RNA access to the PH-like ring and central channel. Structures of Exo10^{Rrp6} and Exo10$^{Rrp44+Rrp6Cterm}$ were compared to query differences that might account for this activity. Whereas the global architecture of the PH-like ring does not differ (Fig. 5d), the Exo9 channel widens in Exo10^{Rrp6} through movement of Rrp4, Rrp40 and Csl4 away from the central channel, widening the gap between Rrp4 and Rrp40 S1 domains by ~4 Å (Fig. 5a–c). Although Exo10^{Rrp6} and Exo10$^{Rrp44+Rrp6Cterm}$ structures are bound to RNA, the increase in channel width in Exo10^{Rrp6} might account for Rrp6-mediated stimulation of Rrp44, especially because Rrp44 and Rrp6 do not physically interact. It remains unclear how Rrp6 exerts this change or if an Exo10^{Rrp44} apo structure differs from its RNA-bound configuration, but it is clear that Rrp6 EXO and CTD are both required for this activity as addition of either element alone is not sufficient to stimulate Exo10^{Rrp44} when added *in trans* (Fig. 5e). These data suggest that the Rrp6 CTD is required to bring the catalytic module in proximity to the S1/KH ring, perhaps eliciting channel widening through EXO domain interaction with Rrp4 and Rrp40. Further data will be required to determine if channel widening is a regulated feature of Exo11$^{Rrp44/Rrp6}$ or if additional cytoplasmic factors elicit channel widening of Exo10^{Rrp44}.

Conclusions

The structure of Exo10^{Rrp6} shows Rrp6 positioned above the Exo9 S1/KH ring while the Exo10$^{Rrp44+Rrp6Cterm}$ structure shows Rrp44 below the PH-like ring. It is notable that Rrp6 activity is altered and becomes dependent on the S1/KH ring when associated with Exo9 (ref. 13). Although shorter RNAs may be directed to Rrp44 via a channel-independent "direct access" route[18], Rrp44 remains highly dependent on the integrity of the central channel throughout both S1/KH and PH-like rings. The dependency on the Exo9 core is remarkable given that both Rrp44 and Rrp6 active sites are exposed to solvent in Exo10^{Rrp6} and Exo10$^{Rrp44+Rrp6Cterm}$ complexes.

That a similar segment of the S1/KH ring is used to engage RNA in opposing directions suggests that overlapping paths to Rrp6 and Rrp44 may serve to commit the exosome to distributive or processive degradation depending on how a particular RNA substrate is delivered to the exosome. Because the paths overlap, the exosome would be unable to interact with another substrate until completing the task at hand. Whereas path choice seems stochastic *in vitro* (Fig. 4d), the nuclear cofactors Mpp6 (ref. 19), Rrp47 (ref. 8) and TRAMP[20] may bias selection of a particular path to facilitate transitions between editing, processing or degradation activities of the exosome.

Rrp6 can stimulate Rrp44 activities when associated with the Exo9 core, perhaps through widening of the S1/KH ring. Channel gating mechanisms as a point of regulation have been described in many systems including, but not limited to, the proteasome[21–25]. Whereas many degradation complexes place their catalytic activities in a protected compartment that is accessed by gating a substrate-responsive channel, the RNA exosome appears inside out, with its catalytic subunits located on the periphery of the exosome core. While the functional relevance of this architecture is not yet clear, it is evident that the exosome core can

©2014 Macmillan Publishers Limited. All rights reserved

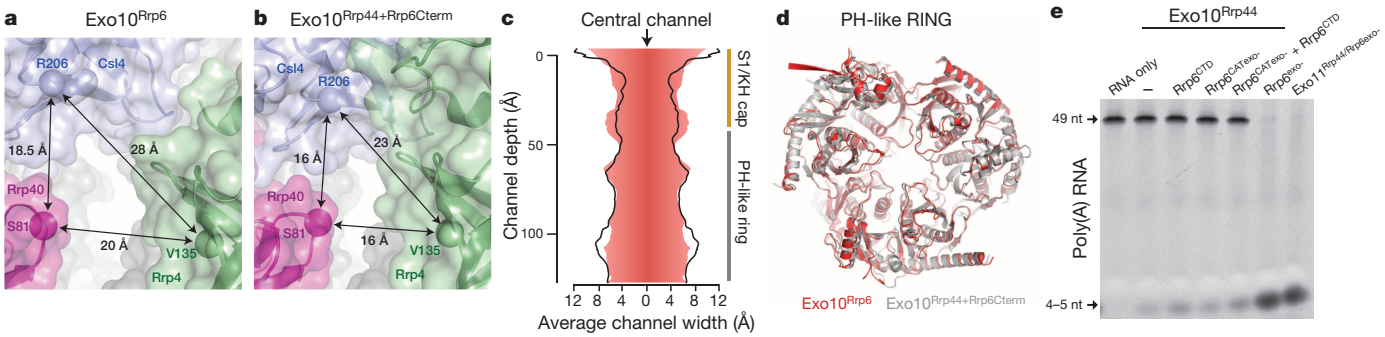


Figure 5 | S1/KH ring widening in Exo10^{Rrp6}. **a**, **b**, Close-up of the central channel looking down the S1/KH ring. Rrp4 (green), Rrp40 (magenta) and Csl4 (light blue) in cartoon with transparent surfaces from Exo10^{Rrp6} (**a**) and Exo10$^{Rrp44+Rrp6Cterm}$ (**b**). Distances indicated between respective labelled amino acids. **c**, Channel dimensions in Exo10^{Rrp6} (red) and Exo10$^{Rrp44+6Cterm}$ (black) calculated using HOLE[28]. **d**, Superposition of PH-like rings for Exo10^{Rrp6} (red) and Exo10$^{Rrp44+6Cterm}$ (grey). **e**, Rrp6^{exo-} (128–733), and not Rrp6^{CTD} (518–733) or Rrp6^{CAT} (128–518), is required to stimulate Rrp44 activity. RNA decay assays conducted at least three times with typical results depicted.

modulate the activities of its catalytic subunits by requiring RNA to pass through distinct elements of the central channel before being processed or degraded.

METHODS SUMMARY

RNA exosome subunits were expressed, purified and reconstituted as described[13,26]; see Methods for details. *S. cerevisiae* Exo10$^{Rrp6exo-}$ (12–14 mg ml^{-1}) was incubated with poly(A)$_{24}$ RNA (Invitrogen) at 1:1.1 molar ratio before crystallization. The structure was solved by molecular replacement. Mutant exosome subunits were generated by PCR-based site-directed mutagenesis. Wild-type and mutant exosome complexes were assayed for RNA degradation activities as described[13]. Ultraviolet crosslinking used catalytically-dead Rrp44 or Rrp6 using conditions described[13].

Online Content Methods, along with any additional Extended Data display items and Source Data, are available in the online version of the paper; references unique to these sections appear only in the online paper.

Received 18 December 2013; accepted 23 April 2014.
Published online 6 July 2014.

1. Wasmuth, E. V. & Lima, C. D. in *The Enzymes* (eds Chanfreau, G.F. & Tamanoi, F.) Ch. 31, 53–76 (Elsevier, 2012).
2. Mitchell, P., Petfalski, E., Shevchenko, A., Mann, M. & Tollervey, D. The exosome: A conserved eukaryotic RNA processing complex containing multiple 3′ to 5′ exoribonucleases. *Cell* **91,** 457–466 (1997).
3. Tomecki, R. *et al.* The human core exosome interacts with differentially localized processive RNases: hDis3 and hDis3L. *EMBO J.* **29,** 2342–2357 (2010).
4. Houseley, J. & Tollervey, D. The many pathways of RNA degradation. *Cell* **136,** 763–776 (2009).
5. Briggs, M. W., Burkard, K. T. & Butler, J. S. Rrp6p, the yeast homologue of the human PM-Scl 100-kDa autoantigen, is essential for efficient 5.8S rRNA 3′ end formation. *J. Biol. Chem.* **273,** 13255–13263 (1998).
6. Yang, W., Lee, J. Y. & Nowotny, M. Making and breaking nucleic acids: two-Mg^{+2} ion catalysis and substrate specificity. *Mol. Cell* **22,** 5–13 (2006).
7. Beese, L. S. & Steitz, T. A. Structural basis for the 3′-5′ exonuclease activity of *Escherichia coli* DNA polymerase I: a two metal ion mechanism. *EMBO J.* **10,** 25–33 (1991).
8. Stead, J. A., Costello, J. L., Livingstone, M. J. & Mitchell, P. The PMC2NT domain of the catalytic exosome subunit Rrp6p provides the interface for binding with its cofactor Rrp47p, a nucleic acid-binding protein. *Nucleic Acids Res.* **35,** 5556–5567 (2007).
9. Callahan, K. P. & Butler, J. S. Evidence for core exosome independent function of the nuclear exoribonuclease Rrp6p. *Nucleic Acids Res.* **36,** 6645–6655 (2008).
10. Midtgaard, S. F. *et al.* Structure of the nuclear exosome component Rrp6p reveals an interplay between the active site and the HRDC domain. *Proc. Natl Acad. Sci. USA* **103,** 11898–11903 (2006).
11. Januszyk, K., Liu, Q. & Lima, C. D. Activities of human RRP6 and structure of the human RRP6 catalytic domain. *RNA* **17,** 1566–1577 (2011).
12. Makino, D. L., Baumgärtner, M. & Conti, E. Crystal structure of an RNA-bound 11-subunit eukaryotic exosome complex. *Nature* **495,** 70–75 (2013).
13. Wasmuth, E. V. & Lima, C. D. Exo- and endoribonucleolytic activities of yeast cytoplasmic and nuclear RNA exosomes are dependent on the noncatalytic core and central channel. *Mol. Cell* **48,** 133–144 (2012).
14. Assenholt, J. *et al.* Exonucleolysis is required for nuclear mRNA quality control in yeast THO mutants. *RNA* **14,** 2305–2313 (2008).
15. Liu, Q., Greimann, J. C. & Lima, C. D. Reconstitution, activities, and structure of the eukaryotic RNA exosome. *Cell* **127,** 1223–1237 (2006).
16. Bonneau, F., Basquin, J., Ebert, J., Lorentzen, E. & Conti, E. The yeast exosome functions as a macromolecular cage to channel RNA substrates for degradation. *Cell* **139,** 547–559 (2009).
17. Drążkowsak, K. *et al.* The RNA exosome complex central channel controls both exonuclease and endonuclease Dis3 activities *in vivo* and *in vitro*. *Nucleic Acids Res.* **41,** 3845–3858 (2013).
18. Liu, J. J. *et al.* Visualization of distinct substrate-recruitment pathways in the yeast exosome by EM. *Nature Struct. Mol. Biol.* **21,** 95–102 (2014).
19. Milligan, L. *et al.* A yeast exosome cofactor, Mpp6, functions in RNA surveillance and in the degradation of noncoding RNA transcripts. *Mol. Cell. Biol.* **28,** 5446–5457 (2008).
20. LaCava, J. *et al.* RNA degradation by the exosome is promoted by a nuclear polyadenylation complex. *Cell* **121,** 713–724 (2005).
21. Makino, D. L., Halbach, F. & Conti, E. The RNA exosome and proteasome: common principles of degradation control. *Nature Rev. Mol. Cell Biol.* **14,** 654–660 (2013).
22. Kish-Trier, E. & Hill, C. P. Structural biology of the proteasome. *Annu. Rev. Biophys.* **42,** 29–49 (2013).
23. Sen, M. *et al.* The ClpXP protease unfolds substrates using a constant rate of pulling but different gears. *Cell* **155,** 636–646 (2013).
24. Effantin, G., Maurizi, M. R. & Steven, A. C. Binding of the ClpA unfoldase opens the axial gate of ClpP peptidase. *J. Biol. Chem.* **285,** 14834–14840 (2010).
25. Cha, S. S. *et al.* Crystal structure of Lon protease: molecular architecture of gated entry to a sequestered degradation chamber. *EMBO J.* **29,** 3520–3530 (2010).
26. Greimann, J. C. & Lima, C. D. Reconstitution of RNA exosomes from human and *Saccharomyces cerevisiae* cloning, expression, purification, and activity assays. *Methods Enzymol.* **448,** 185–210 (2008).
27. The PyMOL Molecular Graphics System, Version 1.5.0.4 Schrödinger, LLC.
28. Smart, O. S., Neduvelil, J. G., Wang, X., Wallace, B. A. & Sansom, M. S. HOLE: a program for the analysis of the pore dimensions of ion channel structural models. *J. Mol. Graph.* **14,** 354–360 (1996).

Acknowledgements We thank NE-CAT beamlines (Advanced Photon Source) supported by P41GM103403 (NIH NIGMS). APS is supported by the US Department of Energy, Office of Basic Energy Sciences, under Contract No. DE-AC02-06CH11357. Beamline X29 (National Synchrotron Light Source) supported by the US Department of Energy, the Office of Basic Energy Sciences and P41RR012408 (NIH NCRR) and P41GM103473 (NIH NIGMS). Research reported in this publication was supported by the National Institute of General Medical Sciences of the National Institutes of Health under award numbers F31GM097910 (E.V.W.) and R01GM079196 (C.D.L.). The content is solely the responsibility of the authors and does not necessarily represent the official views of the National Institutes of Health. C.D.L. is an investigator of the Howard Hughes Medical Institute.

Author Contributions E.V.W. and C.D.L. designed and E.V.W. performed experiments for the *S. cerevisiae* exosomes. E.V.W. and C.D.L. determined the structure. K.J. and C.D.L. designed and K.J. performed the experiments for the *Homo sapiens* exosome. E.V.W. and C.D.L. wrote the manuscript.

Author Information Atomic coordinates and structure factors are deposited in the Protein Data Bank with accession code 4OO1. Reprints and permissions information is available at www.nature.com/reprints. The authors declare no competing financial interests. Readers are welcome to comment on the online version of the paper. Correspondence and requests for materials should be addressed to C.D.L. (limac@mskcc.org).

©2014 Macmillan Publishers Limited. All rights reserved

METHODS

Yeast exosome reconstitution and purification. Expression, purification, and reconstitution of recombinant exosome subunits and complexes have been previously described in detail[13,26]. In brief, the two catalytic subunits (Rrp6 and Rrp44) and nine non-catalytic subunits of the Exo9 core (Rrp41, Rrp45, Rrp42, Mtr3, Rrp46, Rrp43, Rrp4, Rrp40 and Csl4) were cloned as N-terminal 6× histidine Smt3 fusions in pRSFDuet-1 expression vectors (Novagen), and expressed in the *Escherichia coli* expression strain BL21 (DE3) RIL (Stratagene) either as heterodimers (Smt3–Rrp41/Rrp45, Smt3–Rrp42/Mtr3, Smt3–Rrp46/Rrp43) or as distinct subunits (Smt3–Csl4, Smt3–Rrp4, Smt3–Rrp40, Smt3–Rrp6, Smt3–Rrp44). Generation of the Rrp40 and Csl4 point mutants was performed by PCR-mediated site-directed mutagenesis. For the mutant subunits, cells were grown in shaker flasks at 37 °C in Superbroth (Teknova), induced by cold shock on ice, addition of ethanol to a final concentration of 2% and 0.05 mM isopropyl-β-D-thiogalactoside (IPTG), and grown at 18 °C overnight. For all other proteins, cells were grown in shaker flasks at 37 °C in Superbroth and induced by cold shock on ice and addition of 0.4 mM IPTG, and then subjected to shaking at 18 °C overnight. Cells were collected and lysed as described previously. After high-speed centrifugation to pellet the insoluble material, the supernatant was loaded on a nickel-NTA column (Qiagen) and allowed to flow by gravity. After washing with 350 mM NaCl, 20 mM Tris pH 8.0, 1 mM BME, and 20 mM imidazole, the column was further washed with 350 mM NaCl, 50 mM KCl, 20 mM Tris pH 8.0, 1 mM BME, 2 mM ATP, 10 mM $MgSO_4$ to displace chaperone impurities. Protein was eluted with 350 mM NaCl, 20 mM Tris pH 8.0, 1 mM BME, and 250 mM imidazole and then purified by size exclusion chromatography. All subunits were purified on the Superdex 200 (GE) with the exception of Smt3–Csl4 and Smt3–Rrp40, which were purified on a Superdex 75 (GE). Wild-type and mutant subunits eluted at the same volumes on gel filtration. Only Smt3–Rrp6, Smt3–Rrp44, and Smt3–Rrp42/Mtr3 were subjected to overnight cleavage by the SUMO protease Ulp1 (ref. 29) with another step of purification on the Superdex 200 to remove the 6× histidine Smt3 tags; Smt3–Rrp42/Mtr3 was cleaved by Ulp1 before formation of Exo9 as inclusion of this tag interferes with reconstitution. At this stage, subunits were concentrated to 6 to 12 mg ml^{-1} and stored at −80 °C. For reconstitution, Exo9 subunits were mixed together as Smt3 fusions, incubated on ice for 30 min, followed by addition of Ulp1 for another 30 min before overnight dialysis. After purification, exosomes were concentrated to 12–14 mg ml^{-1} and stored at −80 °C in a final buffer of 100 mM NaCl, 20 mM Tris pH 8.0, 0.1 mM $MgCl_2$, 1 mM TCEP.

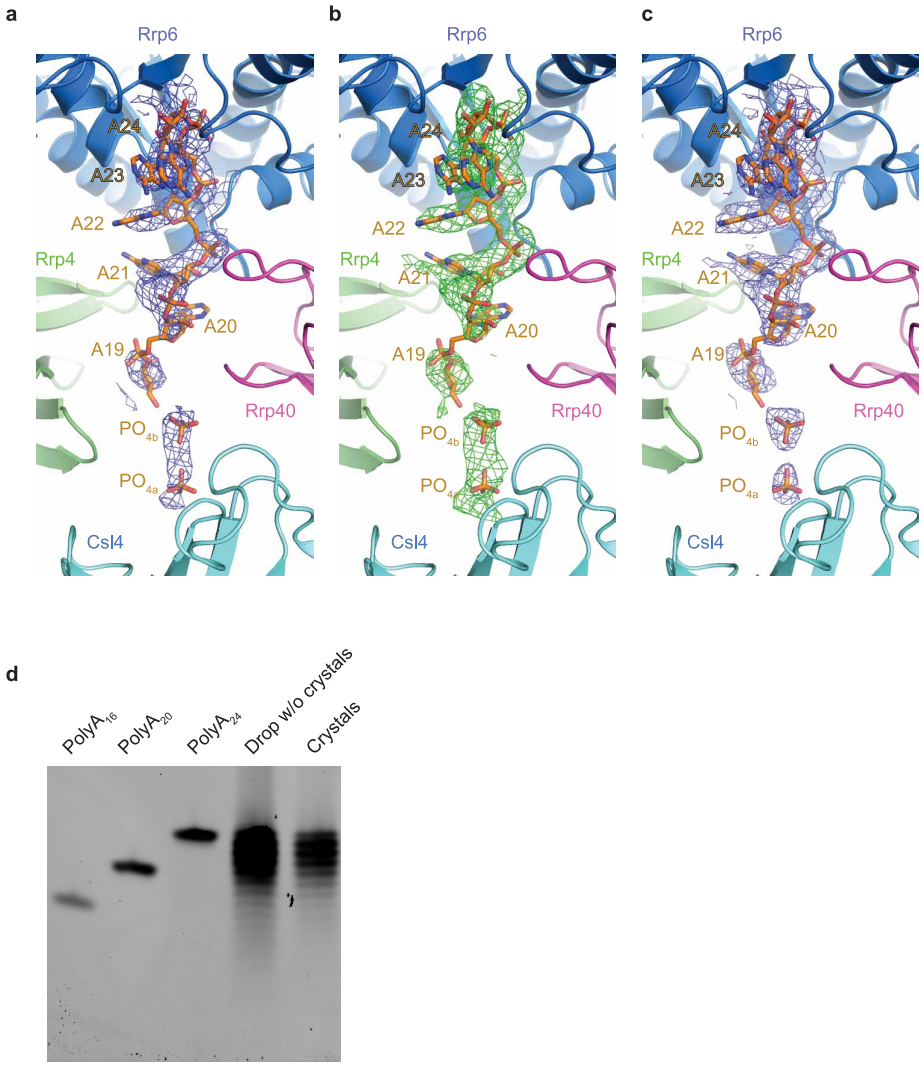
Human exosome reconstitution and purification. For human, expression, purification and reconstitution strategies of the Exo9 core were identical except Smt3–RRP43/MTR3/RRP42 was expressed as a trimer, Smt3–RRP46 was expressed alone (as described previously[15,26]), and $RRP45^{1-302}$/RRP41 was purified with a non-cleavable N-terminal hexa-histidine tag on RRP45. RRP6 (EXOSC10, PM/SCL-100) residues 180 to 804 were PCR-amplified from a previously generated full-length expression construct[11], cloned into pET28a-Smt3 and transformed into BL21 (DE3) RIL. For expression, cells were grown in shaker flasks to ~0.6 $OD_{600\,nm}$, and induced overnight at 18 °C with 0.25 mM IPTG in the presence of 2% ethanol. Subsequent purification of human Smt3–$RRP6^{180-804}$ and reconstitution of $HsExo10^{RRP6}$ is identical to that described for the yeast system. The purification method for the catalytic region, $RRP6^{180-606}$, used for core interaction studies has been described previously[11]. The channel occluding RRP41 and RRP45 mutants were engineered based on those described for *S. cerevisiae*[13], and were generated by PCR to encode electrostatic and steric loop insertions with the primary sequence GTGESEGESES between amino residues Gly 93 and Arg 94 of RRP45 and between Arg 62 and Ala63 of RRP41.

Crystallization and structure determination. Exosome samples were mixed with $poly(A)_{24}$ RNA (Invitrogen) in a 1:1.1 molar ratio and incubated on ice for 1 h before crystallization. Crystals grew at 18 °C by vapour diffusion in either sitting (Greiner Bio One, Crystalquick) or hanging (Hampton Research, VDX) drop formats, in 7–11% PEG3350, 100 mM MES pH 6.7, 4–15% MPD, typically taking 3 to 5 days to appear. Crystals were harvested within 2 weeks. Partial degradation of RNA (20–24 nt) was observed in washed crystals (Extended Data Fig. 1d). For cryoprotection, well solution was replaced with crystallization buffer augmented with 25–30% MPD and crystals were incubated for three days before harvesting; one day before harvest, trays were transferred to 4 °C. A light polarizer was used to exclude multiple crystals and to identify crystals with single regions, which were broken off and flash frozen in liquid nitrogen for data collection. X-ray diffraction data were collected at the Advanced Photon Source 24-ID-E and 24-ID-C beam lines, and the National Synchrotron Light Source X29 beam line. Data was obtained from a single crystal diffracted at NSLS X29 at a wavelength of 1.075 Å at 100 K. Data were processed using HKL2000[30] and statistics reported in Extended Data Table 1 were obtained using Phenix[31] including $CC_{1/2}$ (%) and CC* (%) values of 99.9 (33.8) and 100.0 (71.1) for data between 50–3.3 (3.42–3.3) Å. The structure was solved by molecular replacement using Phaser[32] and coordinates of human apo Exo9 (PDB: 2NN6) and yeast $Rrp6^{CAT}$ (PDB: 2HBL) as search models followed by docking yeast $Exo10^{Rrp44+6Cterm}$ (PDB: 4IFD) (Extended Data Table 1). The structure is refined to R/R_{free} values of 0.227/0.265. The final model includes six nucleotides of the poly(A) 24mer, and two phosphate ions that likely represent the RNA backbone (Extended Data Fig. 1a–c), and 2,751 of the 3,156 amino acids present in the crystal (Extended Data Table 2). The asymmetric unit contains one complex. Iterative rounds of refinement were accomplished using Phenix[31]. RNA and side chains were manually built using O[33] and Coot[34]. The model was initially refined using secondary structure restraints in conjunction with positional refinement followed by individual B-factor refinement. Secondary structure restraints were released and a final round of positional and B-factor refinement was performed followed by refinement of TLS parameters that resulted in a further decrease in R and R_{free} values. Figures depicting the structure were prepared with Pymol[27]. Surface conservation was calculated using ConSurf[35]. Structure quality was assessed using MolProbity[36] indicating the model has excellent geometry with 95.7% in favoured and 100% in allowed regions of Ramachandran space. The structure also scored in the 100th percentile for the Clash and MolProbity scores.

RNA biochemistry. For yeast exosomes, unless otherwise noted, exoribonuclease assays were performed under multiple turnover conditions as described previously[13]. In brief, 10 nM synthetic 49-nt RNAs (Invitrogen) bearing 5′ fluorescein labels were incubated at 30 °C with 1 nM RNA exosome for various time points, and RNA degradation was monitored by resolving reaction intermediates by denaturing TBE-PAGE (Invitrogen), and detected using a Fuji FLA-5000 scanner (FITC filter). A similar protocol was followed for human exosome complexes, the exception being that these assays were performed at 37 °C, with 5 nM of the 49-nt RNA and 50 nM $HsExo10^{RRP6}$. For mix-in experiments (Fig. 5e), twofold molar excess of Rrp6 protein was incubated with $Exo10^{Rrp44}$ on ice for 1 h before initiating RNA decay by addition of RNA. For steady state ultraviolet-RNA crosslinking to 4-thioU-bearing RNAs, 500 nM of exosome complexes with mutations in the exoribonuclease active sites (D238N for Rrp6, D551N for Rrp44) were incubated for 20 min on ice with 50 nM 36-nt 5′ fluorescein RNAs with a single internal 4-thioU (Thermo Scientific) in a 70 µl reaction volume. Binding buffer includes 50 mM KCl, 20 mM Tris pH 8.0, 10 mM DTT, 0.5 mM $MgCl_2$. Crosslinking was performed by subjecting the RNA-exosome mixture to long-range ultraviolet (365 nm) for 15 min in the dark using a 4 W handheld lamp. For the time course described in Fig. 4d, 350 nM of exosome was incubated with 150 nM of RNA, and the binding reactions allowed to proceed for indicated times before initiating crosslinking for 10 min. 15 µl was quenched with LDS loading buffer, and the crosslinked products were separated by SDS–PAGE (Invitrogen) and visualized with a Fuji FLA-5000 scanner (FITC filter). 4-thioU RNA included the following sequences, each of which contained a 5′-fluorescein: 5′-Fl-AAUUAU4thioUUAUUAUUUAUUUAUUAUUUAUUUAUUUAA; 5′-Fl-AAUUAUUUAUUAUU4thioUAUUUAUUAUUUAUUUAUUUAA; 5′-Fl-AAUUAUUUAUUAUUUAUUUAUUAUUUAUU4thioUAUUUAA; 5′-Fl-AAAAAA4thioUAAAAAAAAAAAAAAAAAAAAAAAAAAAA; 5′-Fl-AAAAAAAAAAAAA4thioUAAAAAAAAAAAAAAAAAAAAA; 5′-Fl-AAAAAAAAAAAAAAAAAAAAAA4thioUAAAAAA. For ultraviolet crosslinking to human exosome complexes, samples were incubated with 250 nM of the AU-rich RNA and protein in binding buffer for 60 min on ice, and then placed in a ultraviolet-Stratalinker (Stragene) and subjected to 300,000 µJ of short-wave (254 nm) ultraviolet radiation. Samples were quenched with LDS loading buffer, and crosslinked products were separated and visualized as described above.

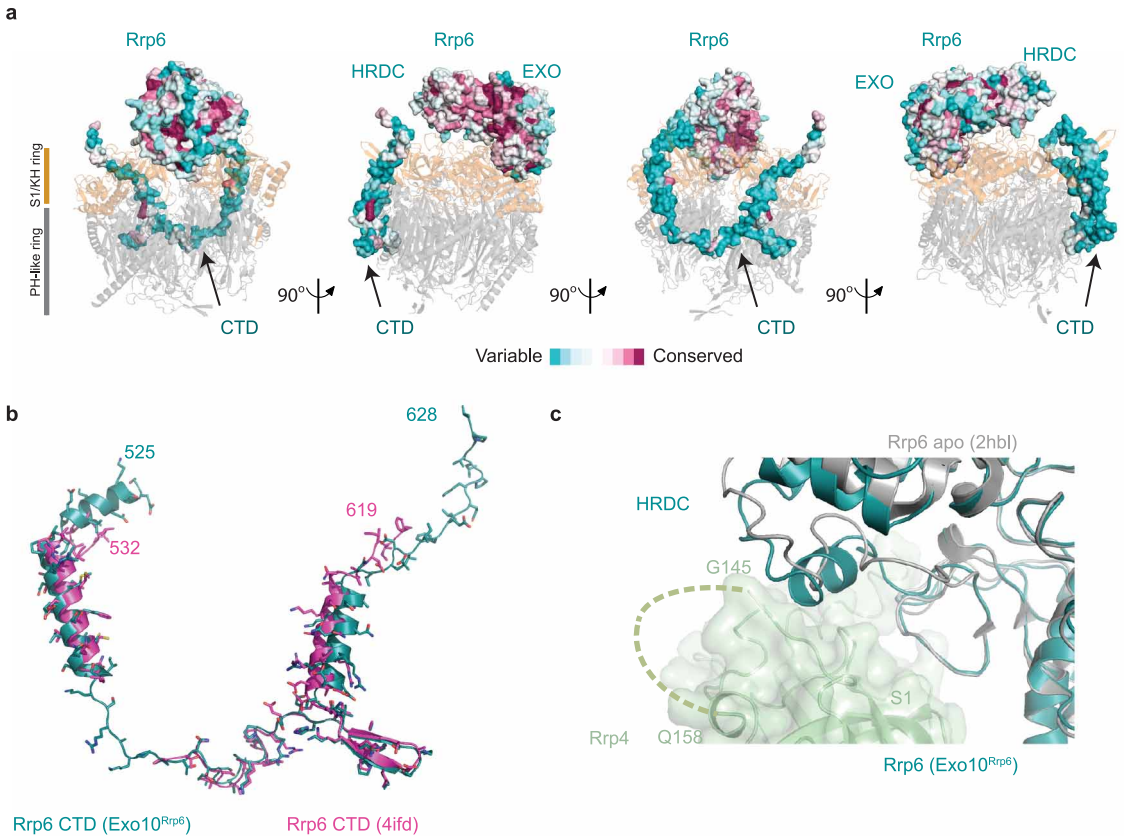
29. Mossessova, E. & Lima, C. D. Ulp1-SUMO crystal structure and genetic analysis reveal conserved interactions and a regulatory element essential for cell growth in yeast. *Mol. Cell* **5,** 865–876 (2000).
30. Otwinowski, Z. & Minor, W. in *Methods in Enzymology* (eds Carter, C. W. Jr & Sweet, R. M.) Vol. 276, 307–326 (Academic Press, 1997).
31. Adams, P. D. *et al.* PHENIX: a comprehensive Python-based system for macromolecular structure solution. *Acta Crystallogr. D* **66,** 213–221 (2010).
32. McCoy, A. J. *et al.* Phaser crystallographic software. *J. Appl. Crystallogr.* **40,** 658–674 (2007).
33. Jones, T. A., Zou, J. Y., Cowan, S. W. & Kjeldgaard, M. Improved methods for building protein models in electron density maps and the location of errors in these models. *Acta Crystallogr. A* **47,** 110–119 (1991).
34. Emsley, P., Lohkamp, B., Scott, W. G. & Cowtan, K. Features and development of Coot. *Acta Crystallogr. D* **66,** 486–501 (2010).
35. Ashkenazy, H., Martz, E., Pupko, T. & Ben-Tal, N. ConSurf 2010: Calculating evolutionary conservation in sequence and structure of proteins and nucleic acids. *Nucleic Acids Res.* **38,** W529–W533 (2010).
36. Chen, V. B. *et al.* MolProbity: all-atom structure validation for macromolecular crystallography. *Acta Crystallogr. D* **66,** 12–21 (2010).

©2014 Macmillan Publishers Limited. All rights reserved



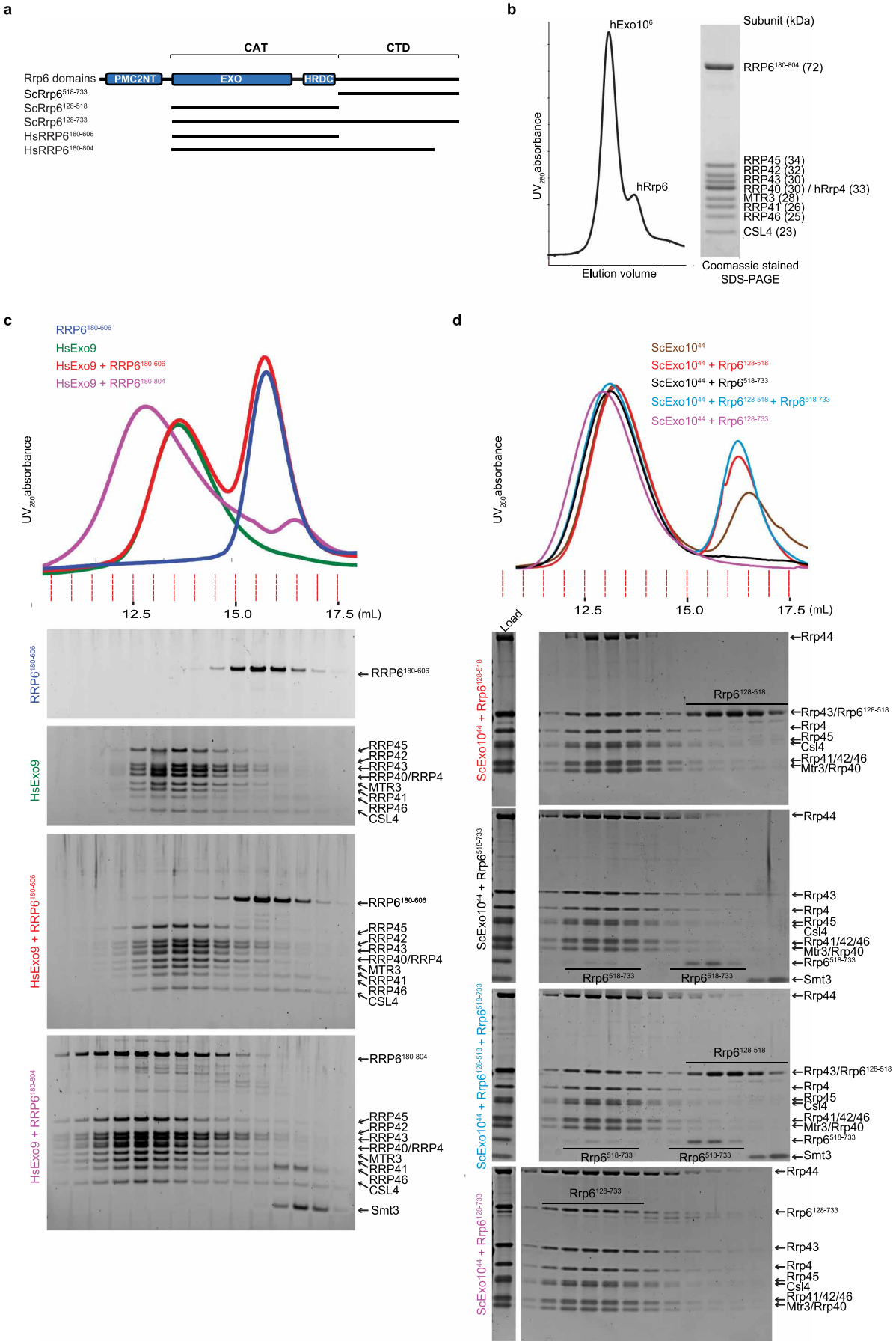
Extended Data Figure 1 | View highlighting electron densities covering RNA in the Exo10^{Rrp6}–poly(A) structure. **a**, Simulated annealing $2F_o - F_c$ omit map contoured at 1.0σ. **b**, Simulated annealing $F_o - F_c$ omit map contoured at 2.0σ. **c**, Final $2F_o - F_c$ omit map contoured at 1.0 σ. RNA and phosphate oxygen, nitrogen, carbon and phosphate atoms are coloured red, blue, orange and dark orange, respectively. Electron density maps shown as wire mesh coloured blue for $2F_o - F_c$ maps and green for the $F_o - F_c$ map. Rrp6, Rrp40, Rrp4 and Csl4 are labelled and shown in cartoon representation in teal, magenta, green and light blue, respectively. **d**, 20 to 24 nucleotides of poly(A) RNA are present in crystals of Exo10^{Rrp6}. Crystals of Exo10^{Rrp6} bound to poly(A)$_{24}$ RNA were first washed by two rounds of transfer to 1 µl well solution, then dissolved in water and TBE-urea sample buffer, and analysed by 15% TBE-urea PAGE. A drop without crystals was run as a control. RNA was stained by Sybr Gold.

©2014 Macmillan Publishers Limited. All rights reserved



Extended Data Figure 2 | Rrp6 features within Exo10^{Rrp6}. **a**, The primary sequence of the catalytic module of Rrp6 (EXO and HRDC) is highly conserved, whereas sequence conservation within the CTD varies. Rrp6 in Exo10^{Rrp6} is represented as a surface, and coloured according to sequence conservation as calculated by ConSurf[35], coloured from red (highly conserved) to blue (variable). The Exo9 core is depicted as a transparent cartoon, with the S1/KH ring in orange, and the PH-like ring in grey. **b**, Superposed structures of the Rrp6 CTD from Exo10^{Rrp6} (residues 525–628; teal) and Exo10$^{Rrp44+Rrp6Cterm}$ (residues 532–557, 565–619; magenta; PDB 4IFD) reveal overall similarity for residues within the respective models. **c**, The conserved linker between the EXO and HRDC domain of Rrp6 adopts an α-helix when associated with the exosome core. Superposition of the Rrp6 catalytic domains from the structures of Exo10^{Rrp6} and Rrp6–AMP (PDB: 2HBL) shows residues Pro 424 to Asn 433 rearrange from a loop in the AMP-bound structure to a helix that is adjacent to a conserved, albeit disordered, loop in the S1 domain of Rrp4. These residues were previously thought to comprise a protein interaction module[10]. Rrp6 is represented as cartoons, with Rrp6 from the Exo10^{Rrp6} structure in teal, and the Rrp6–AMP structure in grey. Rrp4 is in light green and depicted as a cartoon with a transparent surface, with the S1 loop representing residues Gly 145 to Gln 158 shown as a dashed line.

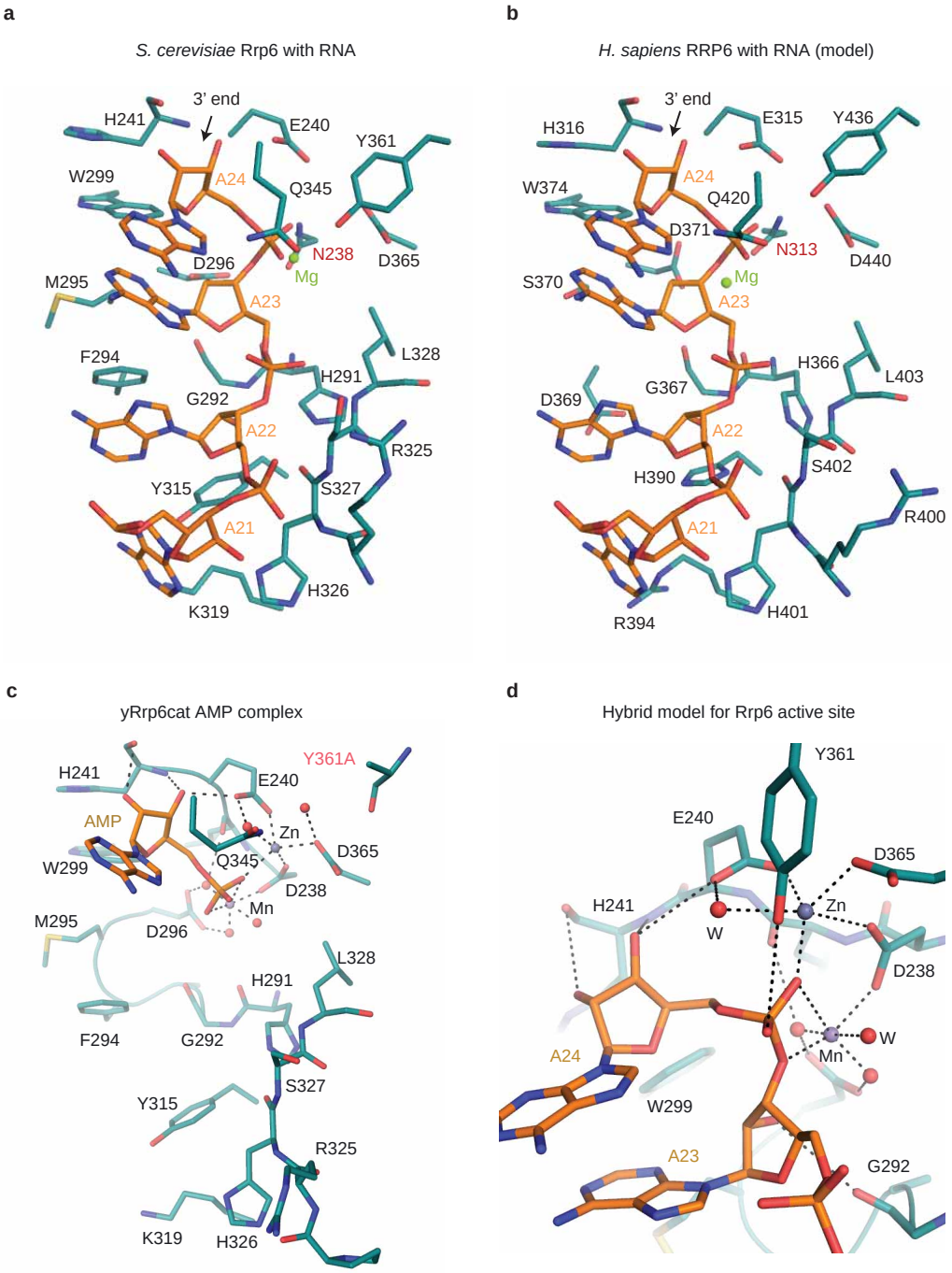
©2014 Macmillan Publishers Limited. All rights reserved



©2014 Macmillan Publishers Limited. All rights reserved

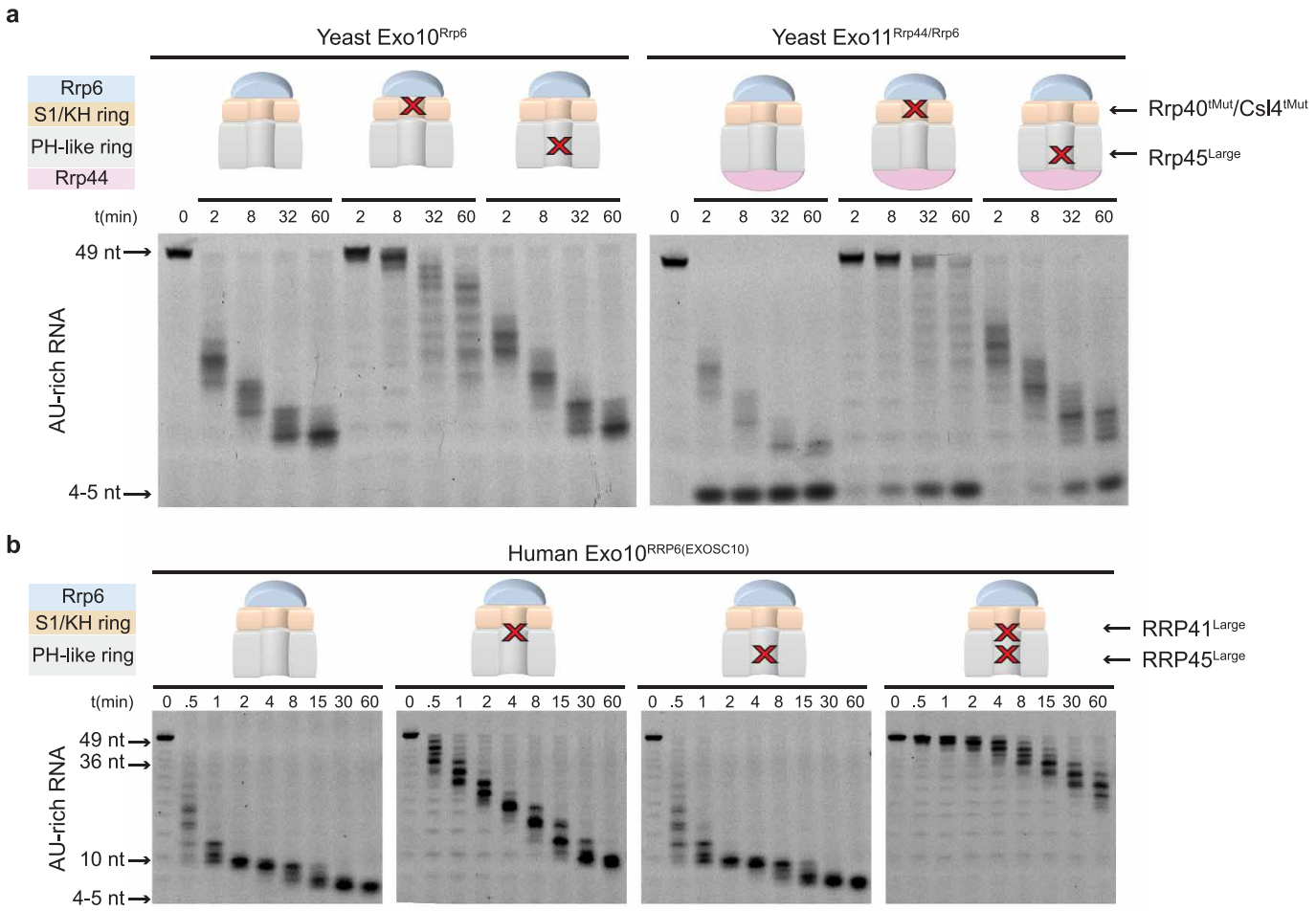
Extended Data Figure 3 | The Rrp6 CTD is required for interaction with human and yeast RNA exosome cores. **a**, Schematic representation of Rrp6 including from N to C terminus the PMC2NT, EXO, HRDC and C-terminal (CTD) domains. EXO and HRDC comprise $Rrp6^{CAT}$. Below are lines representing individual elements used in gel-filtration analysis in **c** and **d** along with amino acid numbering specific for *S. cerevisiae* (Sc) Rrp6 and *Homo sapiens* (Hs) RRP6. **b**, Gel-filtration profile for reconstituted human $Exo10^{RRP6}$ (left) with SDS–PAGE analysis of the peak fractions (right). Subunits labelled in capital letters corresponding to yeast nomenclature for clarity. Apparent molecular weights denoted in kilodaltons. **c**, Interaction studies of human RRP6 with the HsExo9. The human RRP6 catalytic domain (residues 180–606) does not interact well with human Exo9; however, addition of RRP6 180–804 suggests that CTD residues 607–804 are important for stable interaction with Exo9. Reconstitution experiments were performed as described above on mixtures of HsExo9, HsExo9 with twofold excess of $RRP6^{180–606}$ (the catalytic region), HsExo9 with twofold excess of $RRP6^{180–804}$ (the catalytic region with a portion of the carboxy terminus), and $RRP6^{180–606}$. Gel filtration analysis on $RRP6^{180–804}$ in isolation was not possible as this construct is unstable in the absence of the SMT3 tag. Mixtures (0.15 ml at $\sim$2 mg ml^{-1}) were dialysed overnight at 4 °C against reconstitution buffer (50 mM NaCl, 20 mM Tris-HCl pH 8.0, and 10 mM DTT). Mixtures were applied to a Superose 6 10/300 GL column (G.E. Health Sciences) equilibrated with reconstitution buffer with the resulting ultraviolet traces (upper panels) and analysed fractions (lower panel). **d**, Interaction studies of budding yeast Rrp6 with $ScExo10^{Rrp44}$. Rrp6 (residues 128–733) and $Rrp6^{CTD}$, but not $Rrp6^{CAT}$, interact with $Exo10^{Rrp44}$. Rrp6 (residues 128–733), $Rrp6^{CAT}$ (residues 128–518), the $Rrp6^{CTD}$ (residues 518–733), or both were incubated with $Exo10^{Rrp44}$ for one hour on ice before analysis by size exclusion chromatography (Superose 6) in reconstitution buffer. Rrp6 and $Rrp6^{CAT}$ were added in 1.5-fold molar excess to $Exo10^{Rrp44}$, while $Rrp6^{CTD}$ was added in threefold molar excess. For panel **c** and **d**, fractions were analysed by SDS–PAGE and protein detected with Sypro Ruby.

©2014 Macmillan Publishers Limited. All rights reserved



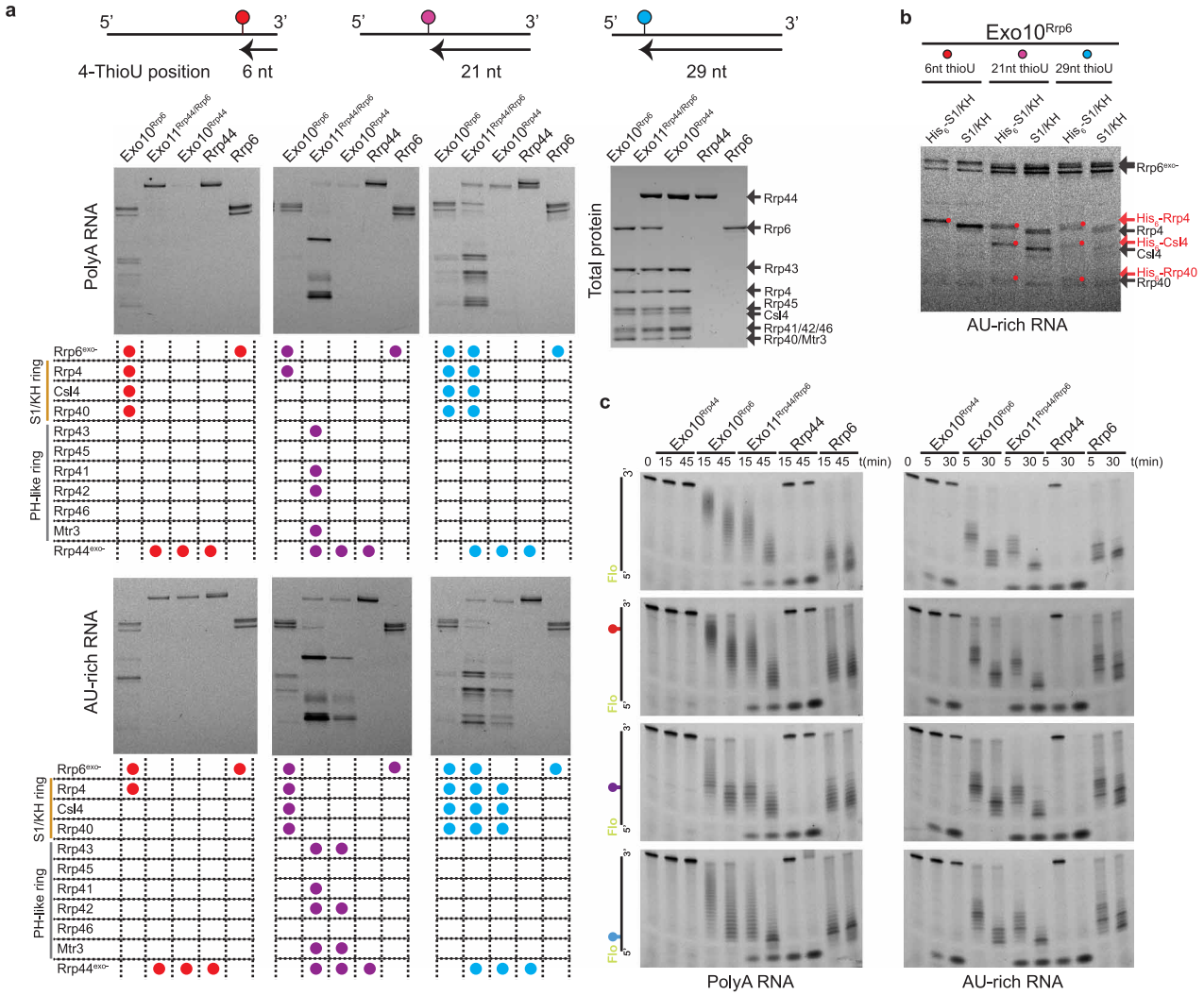
Extended Data Figure 4 | RNA interactions within the Rrp6 active site. **a**, **b**, View of RNA nucleotides 24 to 20 from the 3′ end in the active site of *S. cerevisiae* Rrp6 from the structure of Exo10^{Rrp6} (**a**) and the same RNA modelled into the active site of *H. sapiens* RRP6 (PDB: 3SAF) based on superposing the respective EXO domains (**b**). Residues involved in RNA contacts in the structure of yeast Exo10^{Rrp6} are shown as teal sticks in **a**; the corresponding residues in human are shown in **b**. In both structures, a catalytic aspartate is mutated to asparagine and labelled in red (N238 in yeast; N313 in human). RNA is shown as orange sticks, and magnesium ions are represented as green spheres. **c**, Structure of the yeast Rrp6 catalytic domain in complex with zinc (Zn; blue sphere) and manganese (Mn; yellow sphere) in complex with AMP (PDB 2HBL). Active site residues are depicted as in **a**, **b**. The conserved Tyr 361 side chain was mutated to alanine in this structure (labelled Y361A in red). **d**, Model of the Rrp6 active site constructed by superposing the 3′ nucleotide in the Exo10^{Rrp6} poly(A) structure to the AMP ligand from PDB 2HBL. Amino acid side chains are labelled and putative interactions between metal ligands, active site residues and RNA are depicted by dashed lines.

©2014 Macmillan Publishers Limited. All rights reserved



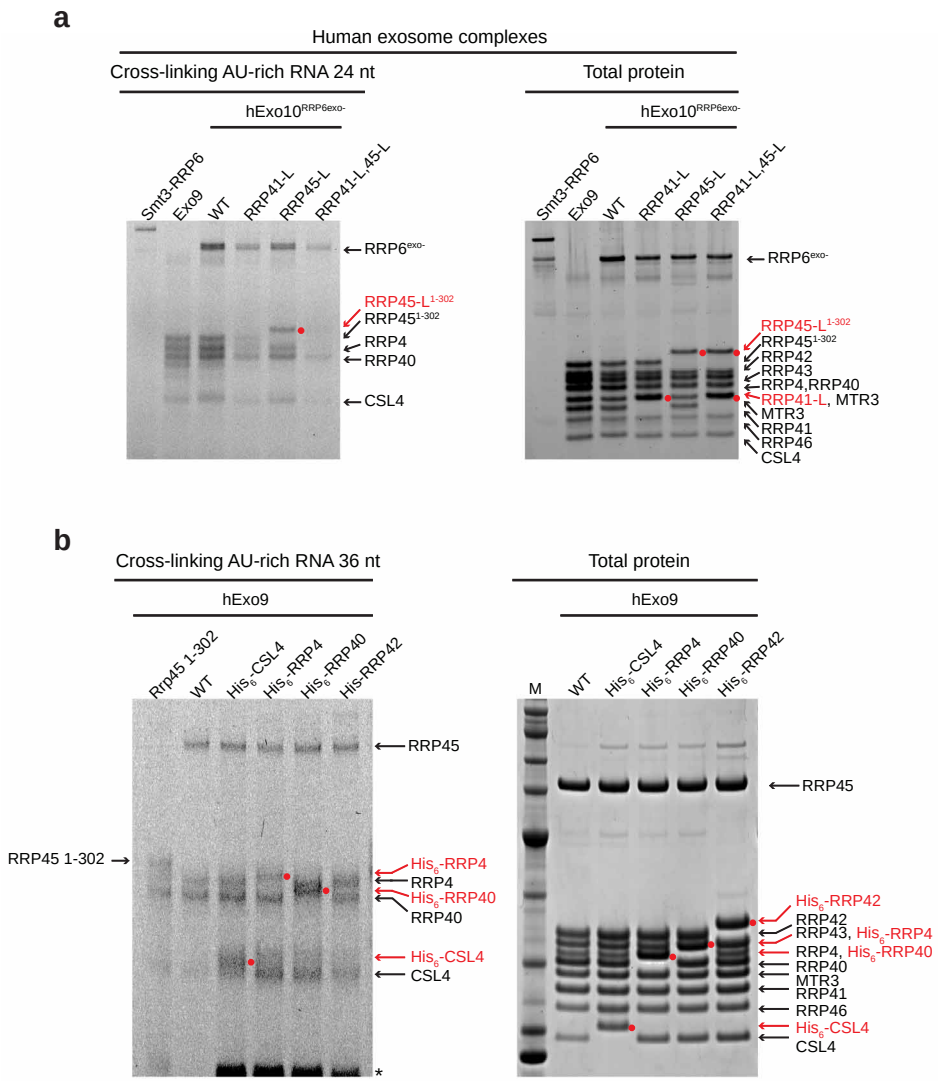
Extended Data Figure 5 | Central channel mutations and their impact on Rrp6 degradation of AU-rich RNA. **a**, 1 nM of reconstituted wild-type and mutant yeast Exo10^{Rrp6} and Exo11$^{Rrp44/Rrp6}$ were incubated with 10 nM 49-nt 5′ fluorescein AU-rich RNA at 30 °C. Reaction intermediates were analysed after indicated time points by denaturing PAGE and imaged with a fluoroimager. Rrp6 activity decreases in the presence of the Rrp40 K107E/K108E/R110D and Csl4 R145A/R150A/R202D mutations in both Exo10^{Rrp6} and Exo11$^{Rrp44/Rrp6}$ but is mostly unaffected by the channel occlusion in the Rrp45^{Large} exosome. Rrp44 exoribonuclease activity is attenuated by mutations in both the S1/KH and PH-like ring in Exo11$^{Rrp44/Rrp6}$. **b**, Exoribonuclease activities of wild-type and mutant forms of human Exo10^{RRP6} were performed with 5 nM 49-nt 5′ fluorescein AU-rich RNA and 50 nM protein at 37 °C. Reaction intermediates were analysed after indicated time points as described in **a**. Mutation studies reveal that the human RRP6 exoribonucleolytic activity decreases in the presence of a channel occlusion near the S1/KH ring (RRP41^{Large}), while a channel occlusion deeper in the central channel (RRP45^{Large}) of HsExo10^{RRP6} has little effect on activity.

©2014 Macmillan Publishers Limited. All rights reserved



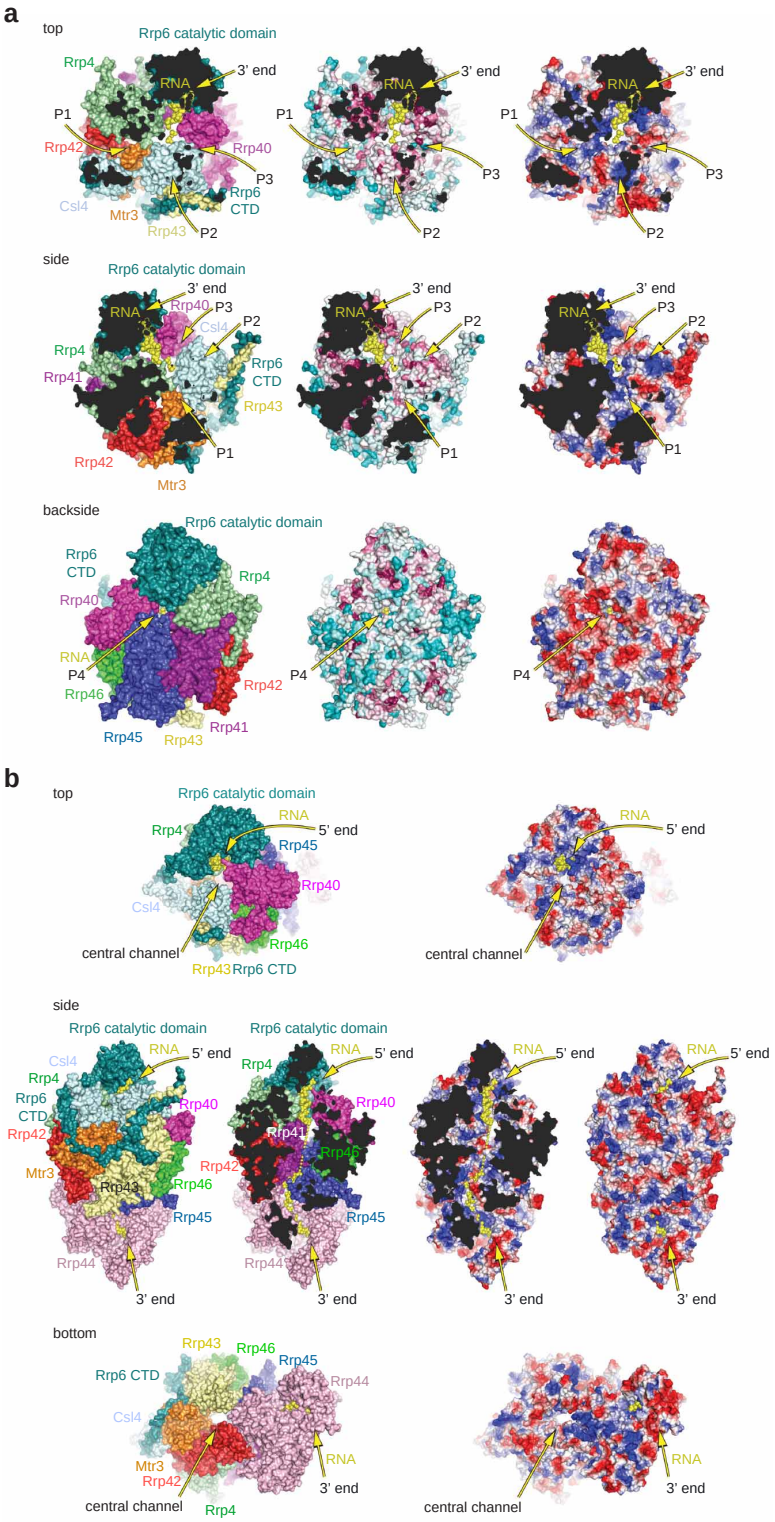
Extended Data Figure 6 | Ultraviolet crosslinking with 36-nt 4-thioU RNAs for yeast exosome complexes. **a**, Raw data used to generate Fig. 4a in main text for poly(A) and AU-rich RNA. See Methods for crosslinking details. Presence or absence of crosslinks to given subunits is summarized in the table and denoted by colour-coded dots, with red corresponding to 4-thioU 6 nt from the 3′ end; purple for 4-thioU 21 nt from the 3′ end; and blue for 4-thioU 29 nt from the 3′ end. **b**, RNA–protein adducts observed in ultraviolet crosslinking to $Exo10^{Rrp6}$ correspond to the S1/KH cap proteins. $Exo10^{Rrp6}$ bearing N-terminal hexahistine tags on the S1/KH cap proteins Rrp4, Rrp40 and Csl4 (ref. 13) or tag-free variants were crosslinked to the three 4-thioU RNAs described above, and resolved by SDS–PAGE and imaged with a fluoroimager. In comparing the His_6-tagged and tagless complexes, mobility shifts are apparent in crosslinks corresponding to the S1/KH cap proteins. **c**, 4-thioU RNAs are bona fide decay substrates for exosome complexes and catalytic subunits, Rrp6 and Rrp44. Conditions using substrate excess (10 nM RNA, 1 nM enzyme), 4-thioU poly(A) RNAs (left) and AU-rich RNAs (right) are comparably degraded to corresponding 36-nt RNAs lacking 4-thioU. Reactions were performed at 30 °C and stopped after indicated time points and resolved by denaturing PAGE and imaged with a fluoroimager. 4-thioU RNAs are colour-coded as in **a** and **b**.

©2014 Macmillan Publishers Limited. All rights reserved



Extended Data Figure 7 | Ultraviolet crosslinking to AU-rich RNA to components of human Exo10^{RRP6}. **a**, Ultraviolet crosslinking of RNA to HsExo10^{RRP6} with open and occluded channels. Human RRP6 (Smt3–RRP6$^{180–804}$), HsExo9 and wild type as well as three different pore occlusion mutants of HsExo10^{RRP6} were incubated and ultraviolet crosslinked to a 24-nt fluorescein-labelled AU-rich RNA substrate. Samples were analysed for the presence of RNA-protein crosslinks (left panel) or integrity of protein via Sypro staining (right panel). Mutant forms of HsExo10^{RRP6} with insertion loops in RRP41-L and RRP45-L are labelled with red asterisks. **b**, Identification of ultraviolet-induced crosslinks. Identification of RNA-protein crosslinks between RNA to cap components of the human Exo9 core (RRP4, RRP40, and CSL4) was facilitated by reconstituting His_6-tagged versions of these subunits into HsExo9 complexes, performing crosslinking assays with a 36-nt fluorescein-labelled AU-rich RNA, and detecting slower mobility for the His_6-tagged crosslinked adducts. Similarly, identification of RRP45-RNA adducts was based on changes in adduct mobility when using isoforms with wild-type carboxy termini (RRP45$^{1–456}$) and the long insertions (RRP45-L$^{1–302}$). RRP6–RNA adducts were determined by crosslinking of a Smt3–RRP6$^{180–804}$ fusion and comparison of 9- and 10-subunit exosomes (in **a**).

©2014 Macmillan Publishers Limited. All rights reserved



Extended Data Figure 8 | RNA paths to Rrp6 and Rrp44. Structure of an Exo11$^{Rrp44/Rrp6}$ model derived by superposing the PH-like ring subunits in Exo10^{Rrp6} and Exo10$^{Rrp44+6Cterm}$ (PDB 4IFD). **a**, RNA paths to the Rrp6 active site. RNA (yellow) shown as derived from the Exo10^{Rrp6} poly(A) complex. Three views are provided from the top, side and backside of the complex with subunits coloured as in Fig. 1 in the main text (left), surfaces coloured according to conservation as calculated by ConSurf[35] (middle) from red (highly conserved) to blue (variable), and surfaces coloured according to electrostatic potential as calculated by Pymol[27] (right). Subunits that are visible are labelled in the left panel as is the RNA. Three putative paths that traverse the S1/KH ring into the Rrp6 active site are denoted by yellow arrows and labels (P1, P2, P3) in the top and side views and a fourth path (P4) under the Rrp6 catalytic domain is denoted in the backside view. Based on conservation, electrostatics and crosslinking we deem P1 or P2 as the most likely path of ingress for the incoming RNA substrate. The top and side views use cutaway surfaces to illustrate the putative paths and surface properties. **b**, RNA paths to the Rrp44 active site. Subunits and surfaces depicted as in **a** with the exception that the RNA is now derived from the structure of Exo10$^{Rrp44+6Cterm}$ (PDB 4IFD) with the RNA edited to remove the stem loop after nucleotide 36. Top, side and bottom views are depicted with the RNA path indicated by a yellow arrow with 5′ and 3′ ends labelled. The position of the central channel is also labelled and indicated by a yellow arrow in the top and bottom views. The top and side views show that RNA could pass by Rrp6 to penetrate the S1/KH and PH-like ring central channel.

©2014 Macmillan Publishers Limited. All rights reserved

Extended Data Table 1 | Data collection and refinement statistics

	Exo10^{Rrp6}/polyA
Data collection	
Space group	$P2_12_12$
Cell dimensions	
a, *b*, *c* (Å)	193.3, 200.1, 97.4
α, β, γ (°)	90.0, 90.0, 90.0
Resolution (Å)	50-3.3 (3.42-3.3) *
R_{merge}	6.1 (65.3)
$I/\sigma I$	15.5 (1.4)
Completeness (%)	97.7 (96.9)
Redundancy	5.2 (3.1)
Refinement	
Resolution (Å)	50-3.3
No. reflections	56332
R_{work}/ R_{free}	22.7/26.5
No. atoms	21595
Protein	21450
Ligand/ion	145
Water	0
B-factors	
Protein	125
Ligand/ion	156
Water	n/a
R.m.s deviations	
Bond lengths (Å)	0.002
Bond angles (°)	0.47

One crystal was used.
*Highest resolution shell is shown in parenthesis.

©2014 Macmillan Publishers Limited. All rights reserved

Extended Data Table 2 | Amino acid and RNA residues

Subunit	Residues	Non-native N-terminal residues	Residues observed in structure
Rrp45	305	None	3-206, 213-301
Rrp41	246	GDPH	4-242
Rrp43	394	None	6-101,121-180, 184-191, 209-249, 271-309, 327-394
Rrp46	223	GS	1-221
Rrp42	265	GDPH	2-161, 170-264
Mtr3	250	None	5-20, 43-147, 163-248
Rrp40	240	GDPH	2-45, 54-235
Rrp4	359	GDPH	5-14, 50-145, 158-249, 277-357
Csl4	292	GDPH	5-70, 105-113, 128-162, 186-291
Rrp6 (128-685)	558	SL	128-516, 525-628
RNA	24	n.a.	19-24

©2014 Macmillan Publishers Limited. All rights reserved